EES Catalysis

PAPER

View Article Online
View Journal | View Issue

Cite this: *EES Catal.*, 2023, 1, 36

Pit-embellished low-valent metal active sites customize CO_2 photoreduction to methanol†

Wei Zhao,[a] Miao Ding,[c] Pengxin Yang,[a] Qiang Wang,[a] Kaifu Zhang,*[a] Xiaowen Zhan,[e] Yu Yu,[a] Qiquan Luo,*[c] Shan Gao,*[a] Jinlong Yang[d] and Yi Xie*[b]

Received 26th August 2022,
Accepted 23rd October 2022

DOI: 10.1039/d2ey00029f

rsc.li/eescatalysis

Customizing catalytic reaction pathways by precisely designing the metal active sites and electron–hole separated channels of metal oxides to simultaneously achieve a high yield and selectivity of photocatalytic CO_2 reduction to liquid fuel remains a challenge. Herein, we for the first time propose that low-valent tungsten sites favor the formation of key CHO* intermediates for highly selective photocatalytic reduction of CO_2 to CH_3OH. *In situ* spectroscopic results and DFT calculations demonstrate that coordinately unsaturated low-valent W sites near the tungsten trioxide (denoted WO_{3-x}) pits serve as catalytic sites and electron capture sites enabling the adsorbed CO_2 to selectively form a predominant lower-energy *CHO intermediate instead of *CO, thereby triggering a unique reaction pathway for CO_2 reduction to CH_3OH. Accordingly, the optimal WO_{3-x} delivers a notable CH_3OH selectivity of up to 86% with a high evolution rate of 17 μmol g^{-1} h^{-1} under sunlight irradiation. This work highlights how low-valent metal active sites in the surface pits can be controlled at the atomic-level to customize the CO_2 reduction reaction (CO_2RR) pathway to generate valuable liquid fuels.

Broader context

Infinite sunlight-driven CO_2 conversion into value-added alternative fuels under mild conditions has emerged as a promising technology to achieve carbon neutrality and ameliorate future energy feedstock supplies. Metal oxides are very promising and efficient catalysts for the photochemical CO_2 reduction to CH_3OH in practical catalytic systems. However, the rapid electron–hole recombination rate and lack of intrinsic catalytic sites in photocatalysts still limit their photocatalytic performance. Therefore, developing a suitable photocatalyst with selective active sites for both the activation of stable CO_2 molecules and the customization of CO_2 reduction products is urgently needed but it remains a challenge. In this tandem experimental–computational work, we propose that the formation of CHO* intermediates at low-valent W sites in the surface pits is the key factor determining selectivity. Furthermore, we demonstrate that the unsaturated W atoms on the WO_{3-x} surface pits are the actual catalytic sites; meanwhile, exposing the low-valent W active site promotes the formation of the *CHO intermediates, thereby facilitating CH_3OH generation. This work highlights product selectivity changes induced by precisely designing the electronic structure of the catalyst surface, while providing deep mechanistic insights into customizing CO_2 reduction to liquid solar fuels.

[a] *Anhui Province Key Laboratory of Chemistry for Inorganic/Organic Hybrid Functionalized Materials, Key Laboratory of Structure and Functional Regulation of Hybrid Materials of Ministry of Education, School of Chemistry and Chemical Engineering, Anhui University, Hefei, 230039, China. E-mail: shangao@ahu.edu.cn, kfzhang@ahu.edu.cn*

[b] *Hefei National Research Center for Physical Sciences at Microscale, University of Science & Technology of China, Hefei, 230026, China. E-mail: yxie@ustc.edu.cn*

[c] *Institutes of Physical Science and Information Technology, Anhui University, Hefei, 230039, China. E-mail: qluo@ustc.edu.cn*

[d] *Hefei National Research Center for Physical Sciences at Microscale, Synergetic Innovation Centre of Quantum Information & Quantum Physics, University of Science & Technology of China, Hefei, 230026, China*

[e] *School of Materials Science and Engineering, Anhui University, Hefei, 230039, China*

† Electronic supplementary information (ESI) available: See DOI: https://doi.org/10.1039/d2ey00029f

Introduction

Converting carbon dioxide (CO_2) to solar fuels *via* naturally inexhaustible solar energy is a sustainable strategy to simultaneously ameliorate energy feedstock supplies and climate change.[1–4] It is known that the CO_2 reduction reaction (CO_2RR) process is quite complex and ambiguous, containing the necessary protonation coupled electron transfer to generate various deoxygenated products.[5–7] Among the possible CO_2RR derivations, the $6H^+/6e^-$ reduction of CO_2 towards CH_3OH, an appealing platform molecule and liquid commodity chemical that can be easily stored and handled, exhibits great potential and economic feasibility for application in industry and organic synthesis, namely 'methanol economy'.[8] In terms of the CO_2RR

process, the metal (M) sites on the photocatalyst surface preferably bond with the C or O atoms in the adsorbed CO_2 through orbital hybridization, resulting in a series of reactive intermediates with the M–C or M–O bond.[9–13] In this regard, the catalyst-reactive intermediate interaction is the key factor determining the performance of photocatalysts in practical catalytic systems. To date, notwithstanding that the most research efforts have shown that semiconductor photocatalysts can generate dominantly CH_4 or CO products with high activity or selectivity during the CO_2RR, only a few reports were on liquid CH_3OH production under comparable conditions.[14,15] More unfortunately, both the selectivity and yield of photocatalytic CO_2-to-CH_3OH reduction remain extremely unsatisfactory due to the high thermodynamic stability of linear CO_2 molecules, rapid recombination kinetics of photogenerated carriers[4,16,17] and multi-electron side reactions with similar reduction potentials.[18] As a promising approach to addressing these issues, developing a suitable photocatalyst with both high activity and selectivity for CO_2 reduction is urgently desired, while it remains a great challenge.

Given that metal oxides are very promising and efficient catalysts, they have been extensively studied for photocatalytic reduction of CO_2 to CH_3OH.[19] As a classical metal oxide photocatalyst, tungsten trioxide (WO_3) seems to be one of the most appropriate candidates to achieve the above goal due to its intriguing advantages such as its beneficial band gap ($\sim$2.6 eV), suitable bandgap edge, strong light harvesting ability, high chemical stability, and excellent photoactivity.[13,20,21] Meanwhile, theoretical calculations further indicate that WO_3 has good CO_2 adsorption and activation abilities, which is the premise of the subsequent reduction reaction.[22,23] However, the rapid electron–hole recombination rate and lack of intrinsic catalytic sites in WO_3 still limit the full utilization of photogenerated charge carriers to initiate the highly selective reduction of CO_2 to CH_3OH. As we all know, constructing surface defects on photocatalysts is an effective strategy to introduce coordinatively unsaturated and catalytically active metal sites and regulate electronic structures.[24,25] This not only promotes local electron delocalization at unsaturated metal sites on the catalyst surface, but also modulates the redox capability of photogenerated charge carriers, activating adsorbed CO_2 molecules and optimizing the reactive intermediates' energy barrier on sites, thereby altering the product selectivity of CO_2 reduction.[26–28] Additionally, to further improve the activity of the catalyst, rational morphology design and precise electron–hole separated channel construction for WO_3 have also offered an opportunity to enable ultra-high specific surface area and expose more accessible active sites, which is beneficial to improving light harvesting while boosting charge carrier separation and migration in the photocatalytic process.[29,30] Nevertheless, as far as we know, the design of highly efficient WO_3 photocatalysts with selective active sites and electron–hole separated channels for customization of the CO_2RR product is still in its infancy and has not been systematically established yet.

On the basis of the above-mentioned considerations, herein, we developed well-defined low-valent W sites to realize highly efficient electron–hole separation and CO_2 activation at single-component WO_{3-x} nanosheet surface pits, thus customizing the CO_2RR pathway to generate CH_3OH. The optimal WO_{3-x} exhibits an impressive CH_3OH evolution rate of 17 μmol g^{-1} h^{-1} with a high selectivity of up to 86% and appreciable stability for 5 consecutive runs. More importantly, the underlying mechanism is further revealed by experimental and computational results, showing that the unsaturated W atoms on the WO_{3-x} surface pits are the actual catalytic sites for CO_2 activation, and the *CO intermediates adsorbed at the active sites are likely to undergo a more rapid and low-energy-barrier protonation process to generate the key *CHO intermediates rather than desorption for CO generation, thereby leading to accelerated catalytic kinetics for CH_3OH production from CO_2 photoreduction.

Results and discussion

It is widely accepted that the introduction of oxygen vacancies or low-valent metal species could modulate the electronic band structure and create trapping sites to benefit separation of photoinduced charge carriers.[31–33] Furthermore, the existence of defects could broaden the light harvesting range and more importantly regulate the local charge density distribution. Thus, we conducted density functional theory (DFT) to check the influence of low-valent W species on the electronic structure of WO_3 and WO_{3-x} (see Calculation details in the ESI†).[34,35] As depicted in Fig. 1a, the Bader charge distribution of the W atom adjacent to the top oxygen vacancy is 2.79 electrons (2.79 e^-) on an optimized WO_{3-x} surface, which is between the charge of W^{6+} (2.97 e^-) in a perfect WO_3 and the charge of W^{4+} (2.27 e^-) in WO_2. This indicates that the localized electron would transfer to W atoms, resulting in a reduced valence state of around +5.[36,37] Interestingly, the low-valent W species on the WO_{3-x} surface exhibits a tremendously enhanced charge density, in which the electron distribution becomes more delocalized, and successively donates its d-orbital electrons to the C═O antibonding orbital (π^*) of adsorbed CO_2 molecules to form highly reactive intermediates. In fact, these intermediates are usually regarded as key factors in redefining the selectivity of the final reduction product.[37] To further unveil the electron-transfer pathway of CO_2 activation on optimized WO_{3-x} surfaces, we applied the charge density difference to track their electron behaviours (Fig. 1b). We found that a crucial *CO intermediate was formed and accumulated on the low-valent WO_{3-x} and perfect WO_3 surface.

In fact, the reaction energy change of this *CO intermediate is a key factor determining the reaction pathway.[37,38] In sharp contrast to the perfect WO_3 surface, there is a strong electron transfer (0.32 e^- lost) from the low-valent W species on WO_{3-x} to the *CO group, and the C–O bond strength is weakened. The weakened C–O bond in the *CO intermediate is stretched from 0.114 to 0.117 nm after introduction of the low-valent W species. This phenomenon indicates that low-valent W species can better stabilize the *CO intermediates and rapidly transfer more electrons to protonate them for production of lower-energy *CHO intermediates during CO_2 photoreduction, thereby changing the reaction pathway to generate CH_3OH instead of CO.

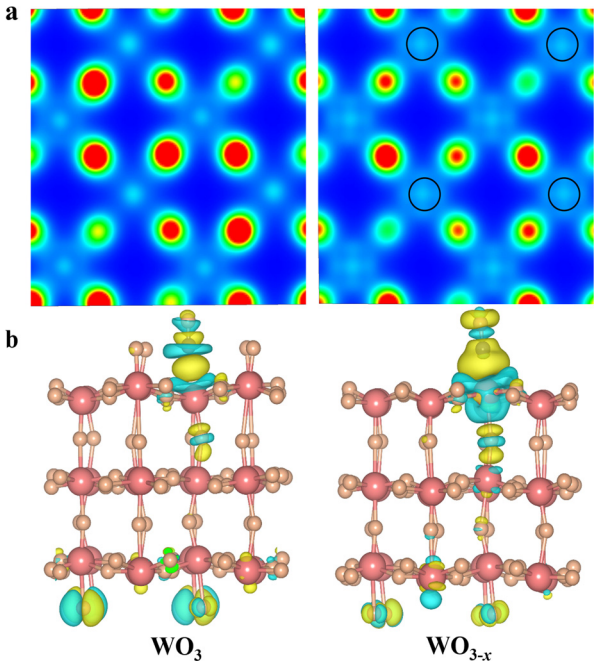

Fig. 1 (a) Distribution of charge density for the original WO_3 (left) and WO_{3-x} (right) plotted from 0 (blue) to 0.035 e^- $bohr^{-3}$ (red). (b) Charge difference diagrams of *CO adsorption on original WO_3 (left) and WO_{3-x} (right); blue and yellow surfaces represent charge depletion and accumulation, respectively.

Inspired by the above analysis, we present that creating favourable atomic-level low-valent W species around the pits on the surfaces of WO_{3-x} nanosheets can remarkably improve the performance of photocatalytic CO_2 reduction. The preparation of WO_{3-x} nanosheet catalysts *via* a two-step method is illustrated in Fig. 2a (see the Experimental section in the ESI† for more details). Initially, the $WO_3{\cdot}H_2O$ precursor was produced using a wet-chemistry approach by adding sodium tungstate dihydrate into nitric acid solution at a certain concentration. The multilayer $WO_3{\cdot}H_2O$ precursor shows a sheet-like morphology and a relatively smooth and flat surface confirmed by the powder X-ray diffraction (XRD) pattern and transmission electron microscopy (TEM) results in Fig. S1 (ESI†). The WO_{3-x} nanosheets with surface pit-decoration and suitable low-valent W sites were subsequently synthesized by an atomic clipping engineering method (Fig. S2, ESI†). The density of low-valent W sites of the WO_{3-x} nanosheets can be adjusted by changing the atmosphere (air or hydrogen) and annealing time. The model catalysts were obtained by calcining the $WO_3{\cdot}H_2O$ precursor at 450 °C for 40 and 60 min in hydrogen or calcined at 700 °C for 5 s in air (denoted H-40, H-60, and A-5), respectively. The XRD pattern shown in Fig. S3 (ESI†) for the obtained products could be indexed to the monoclinic tungsten oxide with a distorted ReO_3^- type unit (JCPDS No. 83-0950). As presented in the Fourier-transform infrared spectroscopy (FT-IR) spectra, the main peaks located at around 743, 811, and 966 cm^{-1} belong to the O–W–O and O–W stretching modes. This result is in good agreement with the XRD results that all as-prepared samples are the pure monoclinic phase of WO_3 (Fig. S4, ESI†). The representative morphology of H-40 is presented in Fig. 2b–d, characterized by TEM and aberration-corrected high-angle annular dark-field scanning transmission electron microscopy (HAADF-STEM). H-40 inherits the two-dimensional sheet-like morphology from the $WO_3{\cdot}H_2O$ precursor and contains numerous highly monodisperse pits. We speculate that the formation of surface pits may be due to the loss of crystal water during pyrolysis. The HAADF-STEM and fast Fourier transform (FFT) images in Fig. 2d and e, respectively, confirm the single crystalline structure and the [001] orientation of H-40. The interplanar spacings of 0.376 and 0.365 nm for H-40 can be assigned to (020) and (200) planes, respectively. In addition, the local (020) interplanar spacing (0.357 nm) in the pits is also smaller than its standard value of monoclinic WO_3 (0.376 nm), further demonstrating the existence of defects in H-40 (Fig. 2f and g). Elemental mappings (Fig. 2c) further confirm a uniform distribution of W and O elements across H-40, which also agrees well with the XRD results. To further confirm the existence of defective structures, a series of spectroelectrochemistry characterization studies were performed. As shown in Fig. 2h, an obvious electron paramagnetic resonance (EPR) signal at g = 2.003 is observed for A-5, H-40, and H-60, which indicates electrons trapped on metal W species. Furthermore, the stronger EPR signal of H-60 confirms the richer low-valent W species formed during material preparation. This result can be further verified by X-ray photoelectron spectroscopy (XPS). Apparently, the deconvolution of the characteristic W 4f band yields two pairs of peaks, corresponding to the W^{6+} (located at 37.6 and 35.5 eV) and W^{5+} (located at 36.5 and 34.3 eV) oxidation states, respectively. Notably, a slightly negative shift of W 4f binding energy and the higher proportion of the peaks at 36.5 and 34.3 eV in H-60, corroborating the existence of more low-valent W^{5+} (Fig. 2i and Fig. S5, Table S1, ESI†).[39–41] This change also affects the electronic structure of oxygen atoms: the H-60 shows the strongest O 1s peak possibly adjacent to the W^{5+} at 531.4 eV (Fig. 2j).[42–44] Furthermore, the Raman bands of H-60 with numerous defective low-valent W^{5+} sites show peak broadening and a redshift compared to the other counterparts, which may be attributed to phonon softening or enhanced electron–phonon coupling at low-valent W sites. All the above mentioned experimental results support the enrichment of low-valent W sites in H-60 (Fig. 2k).

To unravel the influence of unsaturated low-valent W sites on the photocatalytic performance, we probe into the CO_2RR properties of the obtained catalysts. The gaseous and liquid products were quantitatively evaluated by gas chromatography and H nuclear magnetic resonance spectroscopy (Fig. S6–S8, ESI†), respectively. As shown in Fig. 3a, the reduction products on the different obtained catalysts upon illumination are CO, CH_4, and CH_3OH, which gradually accumulated with increasing reaction time. Meanwhile, the $^{13}CO_2$ isotope labelling experiment and a series of control experiments were operated in Ar or without the sample or in the dark to provide direct proof for the origin of the products (Fig. S9, ESI†), and the molecular ion peaks at m/z 17 and 33 were assigned, respectively, to $^{13}CH_4$ and $^{13}CH_3OH$ when $^{13}CO_2$ was used as the reactant, demonstrating that the carbon atoms of the obtained products stemmed from

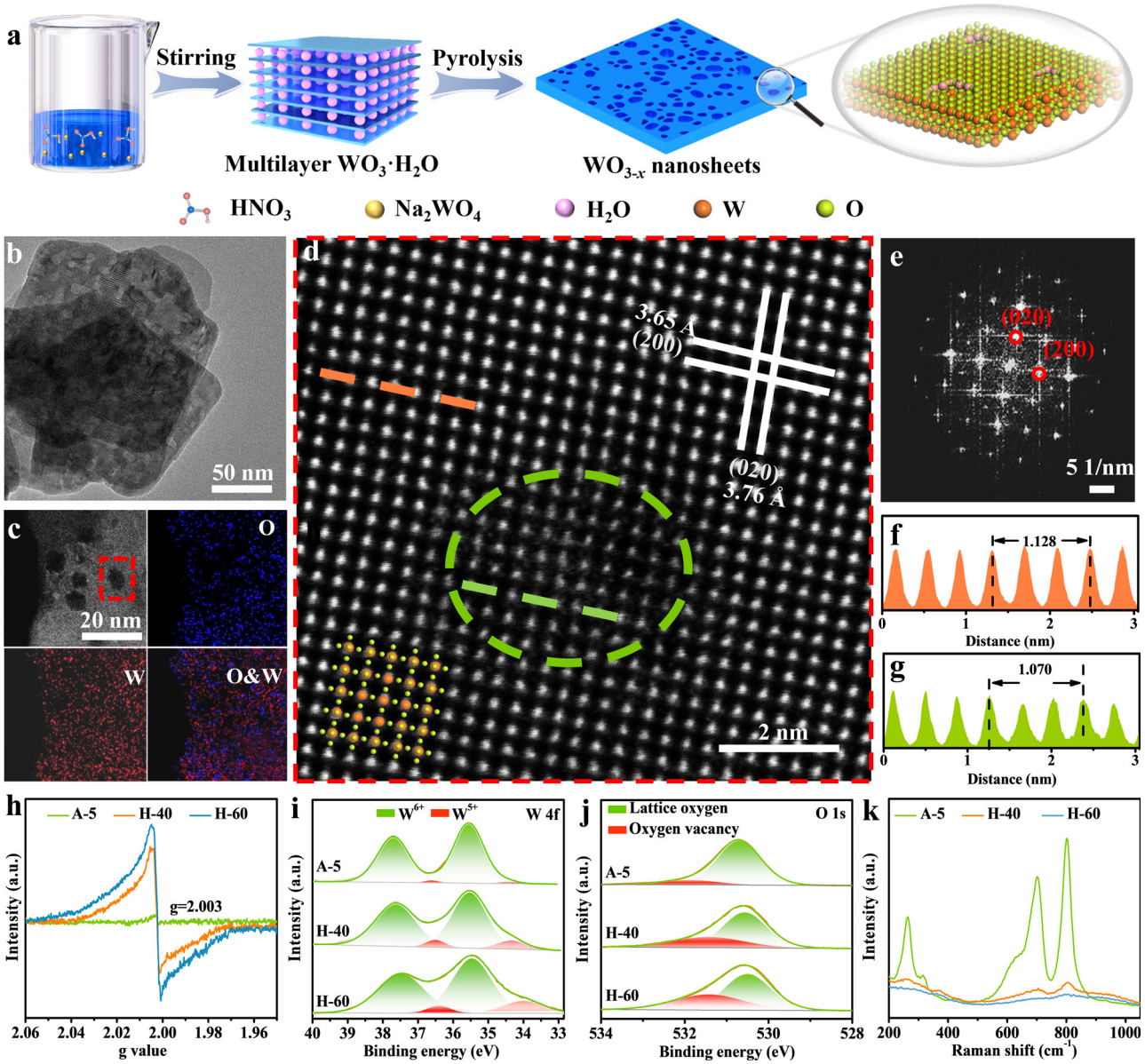

Fig. 2 (a) Schematic illustration of the synthetic process of 2D WO_{3-x} nanosheets. Characterization of the pit-rich WO_{3-x} nanosheets. (b) TEM image, (c) HAADF-STEM EDX elemental mappings, (d) atomic-resolution HAADF-STEM image of H-40, and (e) the corresponding fast Fourier transform (FFT) electron diffraction pattern along the [001] zone axis. (f and g) Intensity distribution measured from the HAADF-STEM image in the perfect crystal face (orange) and pits (green). (h) EPR spectra, (i) W 4f XPS spectra, (j) O 1s XPS spectra and (k) Raman spectra of A-5, H-40, and H-60.

CO_2 feedstock instead of any other impurities.[45,46] Besides, the production of O_2 in the control experiment verified that O_2 stemmed from H_2O (Fig. S10, ESI†). Notably, H-40 manifests the highest CH_3OH production rate of up to 17 μmol g^{-1} h^{-1}, which is about 4.6 times higher than that of the A-5 material. Furthermore, the quantum efficiency (QE) of the H-40 photocatalyst was measured to be as high as ~0.2% under monochromatic visible light (675 nm) irradiation.[47] The trend of the CH_3OH yield agrees well with the photoabsorption of the obtained photocatalysts, demonstrating a high utilization of photogenerated charge carriers (Fig. 3b, 4a and Fig. S11, ESI†). More intriguingly, H-40 achieves the highest CH_3OH selectivity of ~86% among all materials (Fig. 3c). Surprisingly, both the CH_3OH yield and selectivity of the achieved cheap H-40 surpass those of most previously reported state-of-the-art photocatalysts (Fig. 3e).[38,48–60] To further evaluate its stability, H-40 was repeatedly used in the CO_2RR for five cycles and the product yield was tested every 5 h. No obvious variations are observed during measurements, reflecting the high stability of H-40 (Fig. 3d and Fig. S12, ESI†). Besides, XRD, EPR, XPS and TEM measurements of the used H-40 after photocatalysis also support its high structural stability (Fig. S13, S14 and Table S2, ESI†). Clearly, the above results demonstrate that H-40 has high efficiency and selectivity for CO_2 photoreduction, which raises the question: how the density of low-valent W sites in WO_{3-x} thermodynamically and kinetically influences the photocatalytic activity of the CO_2RR?

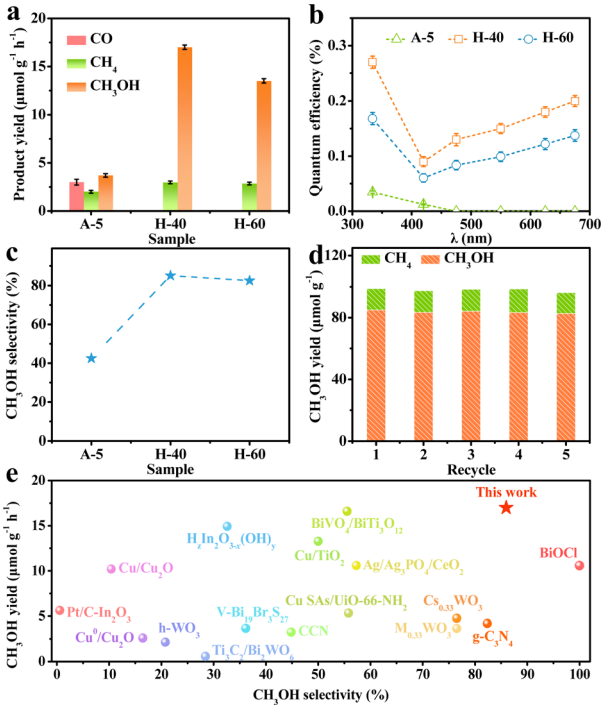

Fig. 3 (a) Product yields of the CO_2RR using the different photocatalysts. (b) QE and (c) CH_3OH selectivity values of different samples. (d) Photocatalytic stability of H-40 for five consecutive runs. (e) Comparison of CO_2RR performance of WO_{3-x} and other reported photocatalysts.

To answer this question, a series of photoelectrochemical characterization studies were conducted to elucidate the excellent CO_2RR activity of the obtained photocatalysts. As shown in Fig. 4a, the existence of low-valent W^{5+} sites results in the formation of abundant internal transition energy levels, which could efficiently narrow the band gap to enhance the visible-light harvesting ability for photocatalytic reactions and tune the sample color range from yellow to dark blue (inset: sample color). The band gaps of A-5, H-40, and H-60 were detected to be 3.18, 2.42, and 2.15 eV, corresponding to their valence band (VB) potentials of 2.61, 1.91, and 1.65 eV (*versus* normal hydrogen electrode, *vs.* NHE) (Fig. 4a and b). Compared with the thermodynamic potential (CO_2/CH_3OH = −0.38 V), the calculated conduction band potential of H-40 is more negative, which is essential to facilitate electron transfer for CO_2 conversion into CH_3OH (Fig. 4c). Furthermore, the formation of pits on the surface significantly enlarged the surface area, which could provide more accessible catalytic sites to improve the catalytic activity. Notably, the numerous low-valent W sites in H-60 significantly improve the light absorption, while the excessive defect sites on the metal oxide surfaces simultaneously generate more photogenerated charge carrier recombination sites for various chemical reactions, resulting in a decrease in catalytic activity.[61,62] Therefore, accurately achieving a suitable density of low-valent W active sites is vital to maximize the photocatalytic activity. This is further verified by the result of the transient photocurrent measurement shown in Fig. 4d, where the enhanced photocurrent of H-40 relative to the other counterparts reveals the promoted generation and separation of photogenerated charge carriers in H-40. The carrier density can be calculated according to the following formula:

$$N_d = (2/e_0\varepsilon_r\varepsilon_0)[d(1/C^2)/dE]^{-1} \quad (1)$$

where e_0 (1.602×10^{-19} C) is the electron charge, C is the capacitance of the space charge layer, N_d is the carrier density, ε_r (20 for WO_3) is the dielectric constant, and ε_0 (8.85×10^{-14} F cm^{-1}) is the vacuum permittivity.[63] The N_d value was calculated to be 3.32×10^{19} cm^{-3}, approximately 7.8 times higher than the 0.4×10^{19} cm^{-3} for A-5 (Fig. 4e and Table S5, ESI†). In addition, the scanning Kelvin probe (SKP) technique was used to probe the work function to determine the electron separation efficiency of the as-prepared photocatalysts. Fig. 4f shows that H-40 achieves the lowest work function value, causing a higher Fermi level of H-40 in comparison with the other counterparts. This means that the built-in electric field and surface energy band bending are enhanced, indicating that a suitable density of low-valent W^{5+} sites is beneficial to improve the efficiency of charge separation. The electrochemical impedance spectroscopy (EIS) further supports the SKP results that H-40 has a lower interfacial charge-transfer resistance resulting from its superior electrical conductivity (Fig. 4g). Meanwhile, the charge separation efficiencies of A-5, H-40, and H-60 nanosheets were characterized by steady-state photoluminescence (PL) emission spectroscopy; the weaker PL intensity of H-40 reveals efficient inhibition of charge recombination (Fig. 4h). Furthermore, transient PL emission spectroscopy was employed to determine the specific charge carrier dynamics of the catalysts. The much slower electron decay kinetics of H-40 reveals a distinctly prolonged lifetime of the photogenerated charge carriers by introducing suitably reduced W^{5+} sites on H-40 (Fig. 4i and Table S4, ESI†).[64–66] All these results provide solid evidence for the proposition that low-valent W^{5+} sites on H-40 can efficiently promote the generation and separation of photoinduced charge carries.

Substantially, the reactant (H_2O and CO_2) adsorption and product desorption on the H-40 surface are crucial during the CO_2RR because the activation and protonation of CO_2 molecules are involved. As revealed by the N_2 adsorption and desorption curves shown in Fig. S15 and S16a (ESI†), moderate pits decorated on H-40 enable a higher surface area, more low-valent W^{5+} sites, and more electron–hole separation channels, and stabilize more key active species to a certain extent, which can promote the adsorbate on its surface for subsequent surface redox reactions. As expected, H-40 with larger surface area exhibits higher CH_3OH activity and selectivity. CO_2 temperature-programmed desorption (CO_2-TPD) shows a similar adsorption ability to the obtained samples (Fig. S16b, ESI†). The enhanced peaks of H-40 at higher temperatures indicate that the existence of suitable low-valent W^{5+} sites can dramatically promote the chemisorption ability of CO_2. Moreover, this result is further reinforced by the contact angle measurements (Fig. S17, ESI†). Hence, all these results demonstrate that the introduced coordination unsaturated low-valent W^{5+} sites endow it with higher surface hydrophilicity and enhanced CO_2 adsorption capacity.

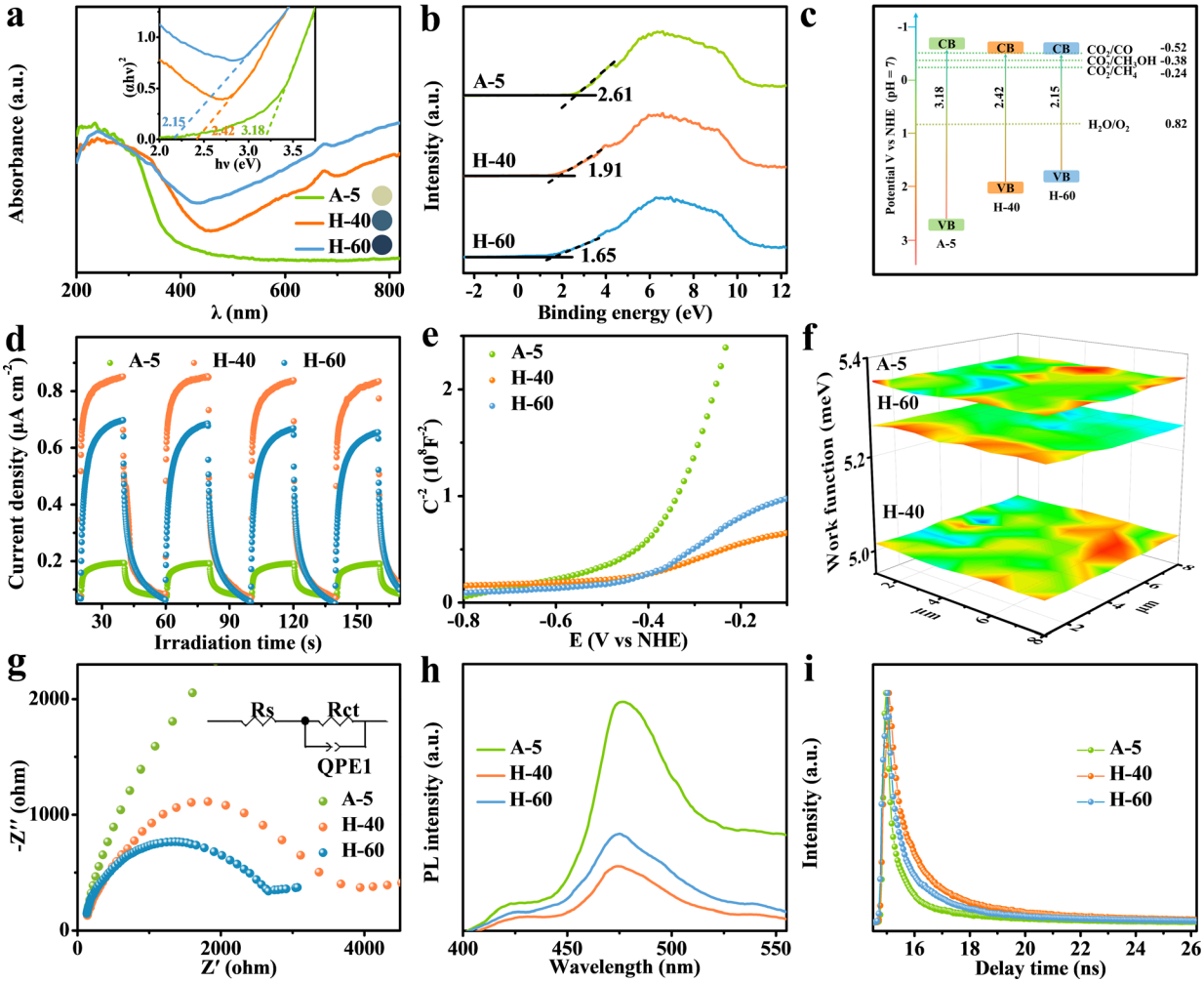

Fig. 4 (a) UV-vis absorption spectra (inset: Tauc plots), (b) VB XPS spectra, (c) energy band structure alignments, (d) transient photocurrent responses (0.5 V *vs.* Ag/AgCl, pH 7), (e) Mott–Schottky plots, (f) SKP maps, (g) EIS spectra, (h) steady-state PL spectra, and (i) time-resolved transient PL decay of A-5, H-40, and H-60, respectively.

Achieving excellent activity and controllable product selectivity for CO_2 photoreduction is generally considered as the bottleneck because of the complicated and sluggish multielectron transfer processes. To probe the evolution of the adsorbed active intermediates on the obtained catalyst surface, *in situ* FT-IR characterization was performed to track the dynamics process of the CO_2RR. As for H-40 (Fig. 5a), the emergence of infrared peaks at 1051, 1430, 1623, and 2065 cm^{-1} can be assigned to *CHO, HCO_3^*, *COOH, and *CO species, as well as two peaks at 2962 and 1197 cm^{-1} corresponding to *OCH_3 species; in the meantime, the CH_3OH peak of the target product at 2850 cm^{-1} was also observed, consistent with previously reported studies,[67–69] and these peak intensities gradually strengthened as a function of irradiation time from 0 to 25 min. Among them, the major preponderant *CHO species is generally regarded as the most significant intermediate during the photocatalytic CO_2-to-CH_3OH reduction process. It is worth noting that the energy levels of key reactive intermediate species on the catalyst surface can determine whether an easy or complex reaction pathway is present. As expected, the surface coverage of *CHO species on H-40 is much larger relative to other samples, leading to high CH_3OH selectivity and a superior yield (Fig. S18, ESI†). Therefore, we deduce that the most likely reaction path for the CO_2-to-CH_3OH reduction process is outlined below:

$$CO_2(g) \rightarrow *CO_2 \quad (R1)$$

$$H_2O \rightarrow H^+ + OH^- \quad (R2)$$

$$*CO_2 + H^+ + e^- \rightarrow *COOH \quad (R3)$$

$$*COOH + H^+ + e^- \rightarrow *CO + H_2O \quad (R4)$$

$$*CO + H^+ + e^- \rightarrow *CHO \quad (R5)$$

$$*CHO + H^+ + e^- \rightarrow *OCH_2 \quad (R6)$$

$$*OCH_2 + H^+ + e^- \rightarrow *OCH_3 \quad (R7)$$

$$*OCH_3 + H^+ + e^- \rightarrow *OHCH_3 \quad (R8)$$

where * denotes the active sites of the catalysts.

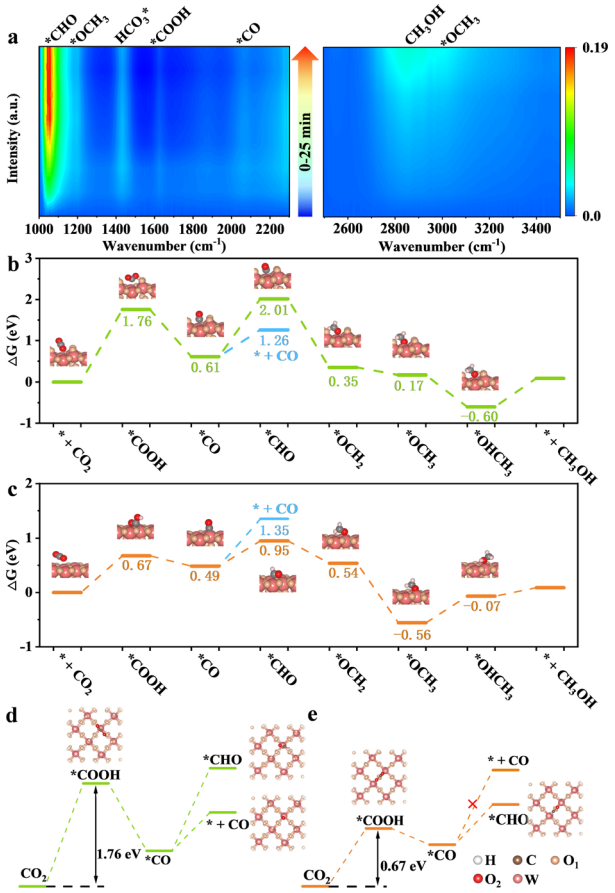

Fig. 5 (a) *In situ* FT-IR spectra of H-40. Free energy diagrams for reduction of CO_2 to CH_3OH over (b) WO_3 and (c) WO_{3-x} based on DFT calculation as well as the corresponding structure models for every reaction step. Key steps of CO_2 photoreduction of (d) WO_3 and (e) WO_{3-x}. White, dark brown, light yellow, red and pink balls indicate H, C, O (in WO_3), O (in CO_2) and W atoms, respectively.

To further verify our hypothesis, the remarkable selectivity of the low-valent W^{5+} mediated WO_3 (WO_{3-x}) catalyst was examined by DFT simulation, in which the structural model based on the (001) facet of WO_3 was employed. The Gibbs free energy profiles and their optimized reactive intermediate adsorption configurations of each possible step for CO_2 reduction to CH_3OH on the surface of the perfect WO_3 and WO_{3-x} are displayed in Fig. 5b–d. Take the perfect WO_3 as an example; the potential-determining step (PDS) is CO_2 protonation to generate *COOH with a reaction free-energy-barrier of 1.76 eV. After the introduction of the low-valent W species, this PDS has a lower *COOH formation energy of 0.67 eV, which facilitates the whole reaction. This result indicates that the different adsorption sites likely have a decisive influence on the formation energies of crucial intermediates.[33]

To clarify this, we performed a precise analysis of the above two models and found a very clear difference in the step of protonation of the *CO intermediate to generate *CHO. Most interestingly, we also find that the *CHO formation energy is higher than the desorption energy of the CO molecules on the perfect WO_3, while the CO desorption energy and *CHO formation energy on WO_{3-x} are diametrically opposite. This change might indicate that the low-valent W species induced the redistribution of the photogenerated electrons on the WO_{3-x} surface, thereby efficiently stabilizing and promoting the protonation of *CO to generate *CHO instead of desorbing CO molecules from its surface, which is also supported by the *in situ* FT-IR results.[30,70] Furthermore, the CO-TPD isotherm (Fig. S19, ESI†) confirms the fact that the introduction of suitable low-valent W sites can regulate the CO adsorption and desorption capacity to a certain extent, thereby favouring the subsequent CO protonation and relieving the CO poisoning. This result further suggests that appropriate defect density is critical for customizing liquid products. More importantly, the desorption energy of the CH_3OH molecules on the WO_{3-x} surface is much lower than that on the perfect WO_3 surface, indicating that suitable low-valent W species are more beneficial for the CH_3OH desorption process and efficiently boost its activity and selectivity. The above results demonstrate that the suitable surface pit-embellished low-valent W sites in the WO_{3-x} system could modulate the reaction intermediate's formation energy to change the reaction pathway, which accounts for highly selective photocatalytic CO_2 reduction to CH_3OH.

Conclusions

In summary, we proposed a general strategy to prepare an extremely efficient WO_{3-x} catalyst and elucidated the origin of its superior CO_2RR activity. More specifically, the unique WO_{3-x} nanosheets with abundant surface pits promoted the creation of low-valent W sites to interact with the adsorbed reactant. *In situ* FT-IR spectra and computational results demonstrate that the delocalized charge near the low-valent W sites not only reduces the reaction energy for CO_2 transformation into the key *CHO intermediate, but also regulates the energy level of reaction intermediates to prevent the production of other multi-electron carbon-based products, which is a key characteristic for achieving high CH_3OH selectivity. Consequently, a suitable low-valent W concentration enables the H-40 catalyst to show a drastically enhanced yield of CH_3OH as well as appreciable stability, which outperformed most previously reported state-of-the-art photocatalysts operated under similar conditions. This work puts forward some inspirations for the rational design of surface electronic structures of photocatalysts and the precise control of the reaction pathways, while providing deep mechanistic insights into customizing the conversion of CO_2 into valuable solar fuels.

Author contributions

Y. X. and S. G. conceived and designed the research. W. Z., P. X. Y. and Q. W. carried out the experiments. J. L. Y., Q. Q. L. and M. D. conducted the DFT calculations. K. F. Z., X. W. Z. and Y. Y. participated in the experimental data analyses and scientific discussions. S. G. and K. F. Z. wrote the manuscript. W. Z., M. D., and P. X. Y. contributed equally to this work.

Conflicts of interest

There are no conflicts to declare.

Acknowledgements

The work was supported by the National Natural Science Foundation of China (grants U1832189, U21A20317, 22288201, 22205002 and 22103001), the research start-up fund from Anhui University (S020118002/060, S020318008/016) and the University Synergy Innovation Program of Anhui Province (GXXT-2020-001). The DFT calculations were performed in the Supercomputing Center of Anhui University and the National Supercomputing Center in Shanghai.

References

1 X. Jiang, J. Huang, Z. Bi, W. Ni, G. Gurzadyan, Y. Zhu and Z. Zhang, *Adv. Mater.*, 2022, **34**, 2109330.
2 J. W. Wang, L. Jiang, H. H. Huang, Z. Han and G. Ouyang, *Nat. Commun.*, 2021, **12**, 4276.
3 Y. Yamazaki, M. Miyaji and O. Ishitani, *J. Am. Chem. Soc.*, 2022, **144**, 6640–6660.
4 Y. A. Wu, I. McNulty, C. Liu, K. C. Lau, Q. Liu, A. P. Paulikas, C.-J. Sun, Z. Cai, J. R. Guest, Y. Ren, V. Stamenkovic, L. A. Curtiss, Y. Liu and T. Rajh, *Nat. Energy*, 2019, **4**, 957–968.
5 E. Gong, S. Ali, C. B. Hiragond, H. S. Kim, N. S. Powar, D. Kim, H. Kim and S.-I. In, *Energy Environ. Sci.*, 2022, **15**, 880–937.
6 Y. Birdja, E. Pérez-Gallent, C. Figueiredo, J. Göttle and T. Koper, *Nat. Energy*, 2019, **4**, 732.
7 L. Yuan, M. Y. Qi, Z. R. Tang and Y. J. Xu, *Angew. Chem., Int. Ed.*, 2021, **60**, 2–25.
8 S. Navarro-Jaén, M. Virginie, J. Bonin, M. Robert, R. Wojcieszak and A. Y. Khodakov, *Nat. Rev. Chem.*, 2021, **5**, 564–579.
9 Z. Zhang, X. Ding, X. Yang, W. Tu, L. Wang and Z. Zou, *EcoMat*, 2021, **3**, 12078.
10 J. Li, Y. Zhao, M. Xia, H. An, H. Bai, J. Wei, B. Yang and G. Yang, *Appl. Catal., B*, 2020, **261**, 118244.
11 R. Yang, J. Duan, P. Dong, Q. Wen, M. Wu, Y. Liu, Y. Liu, H. Li and T. Zhai, *Angew. Chem., Int. Ed.*, 2022, **61**, e202116706.
12 Y. Yang, Y. Pan, X. Tu and C. Liu, *Nano Energy*, 2022, **101**, 107613.
13 J. Duan, T. Liu, Y. Zhao, R. Yang, Y. Zhao, W. Wang, Y. Liu, H. Li, Y. Li and T. Zhai, *Nat. Commun.*, 2022, **13**, 2039.
14 Y. Feng, C. Wang, P. Cui, C. Li, B. Zhang, L. Gan, S. Zhang, X. Zhang, X. Zhou, Z. Sun, K. Wang, Y. Duan, H. Li, K. Zhou, H. Huang, A. Li, C. Zhuang, L. Wang, Z. Zhang and X. Han, *Adv. Mater.*, 2022, **34**, 2109074.
15 H. Wang, L. Zhang, K. Wang, X. Sun and W. Wang, *Appl. Catal., B*, 2019, **243**, 771–779.
16 Z. Zhang, X. Ding, X. Yang, W. Tu, L. Wang and Z. Zou, *EcoMat*, 2021, **3**, 12078.
17 Z. Zhang, J. Liu, J. Wang, Q. Wang, Y. Wang, K. Wang, Z. Wang, M. Gu, Z. Tang, J. Lim, T. Zhao and F. Ciucci, *Nat. Commun.*, 2021, **12**, 5235.
18 L. Xiao, X. Xu, Y. Jia, G. Hu, J. Hu, B. Yuan, Y. Yu and G. Zou, *Nat. Commun.*, 2021, **12**, 318.
19 K. A. Goulas, A. V. Mironenko, G. R. Jenness, T. Mazal and D. G. Vlachos, *Nat. Catal.*, 2019, **25**, 5096–5099.
20 G. Yang, X. Zhu, G. Cheng, R. Chen, J. Xiong, W. Li and Y. Wei, *J. Mater. Chem. A*, 2021, **9**, 22781–22809.
21 H. Zhang, Y. Wang, S. Zuo, W. Zhou, J. Zhang and X. W. D. Lou, *J. Am. Chem. Soc.*, 2021, **143**, 2173–2177.
22 J. Yan, T. Wang, G. Wu, W. Dai, N. Guan, L. Li and J. Gong, *Adv. Mater.*, 2015, **27**, 1580–1586.
23 Y. Zhao, Z. Han, G. Gao, W. Zhang, Y. Qu, H. Zhu, P. Zhu and G. Wang, *Adv. Funct. Mater.*, 2021, **31**, 2104976.
24 Y. Sun, Q. Liu, S. Gao, H. Cheng, F. Lei, Z. Sun, Y. Jiang, H. Su, S. Wei and Y. Xie, *Nat. Commun.*, 2013, **4**, 2899.
25 B. Zhang, J. Zhang, M. Hua, Q. Wan, Z. Su, X. Tan, L. Liu, F. Zhang, G. Chen, D. Tan, X. Cheng, B. Han, L. Zheng and G. Mo, *J. Am. Chem. Soc.*, 2020, **142**, 13606–13613.
26 S. Li, L. Meng, W. Tian and L. Li, *Adv. Energy Mater.*, 2022, **32**, 2200629.
27 Z. Xiao, C. Xie, Y. Wang, R. Chen and S. Wang, *J. Energy Chem.*, 2021, **53**, 208–225.
28 Z. Yang, T. Sander, J. Gebhardt, T. A. Schaub, J. Schönamsgruber, H. R. Soni, A. Görling, M. Kivala and S. Maier, *ACS Nano*, 2020, **14**, 16887–16896.
29 B. Wu, L. Zhang, B. Jiang, Q. Li, C. Tian, Y. Xie, W. Li and H. Fu, *Angew. Chem., Int. Ed.*, 2021, **60**, 4815–4822.
30 Y. Liu, L. Liang, C. Xiao, X. Hua, Z. Li, B. Pan and Y. Xie, *Adv. Energy Mater.*, 2016, **6**, 1600437.
31 T. W. Kim, Y. Ping, G. A. Galli and K. S. Choi, *Nat. Commun.*, 2015, **6**, 8769.
32 T. Yan, N. Li, L. Wang, Q. Liu, A. Jelle, L. Wang, Y. Xu, Y. Liang, Y. Dai, B. Huang, J. You and G. A. Ozin, *Energy Environ. Sci.*, 2020, **13**, 3054–3063.
33 L. W. Zhang, L. Wang and Y. F. Zhu, *Adv. Funct. Mater.*, 2007, **17**, 3781–3790.
34 G. Wang, Z. Chen, T. Wang, D. Wang and J. Mao, *Angew. Chem., Int. Ed.*, 2022, **61**, e202210789.
35 G. Moore, S. Howell, M. Brady, X. Xu and K. McNeil, *Nat. Commun.*, 2021, **12**, 1–9.
36 Y. Mao, P. Wang, L. Li, Z. Chen, H. Wang, Y. Li and S. Zhan, *Angew. Chem., Int. Ed.*, 2020, **59**, 3685–3690.
37 X. Li, Y. Sun, J. Xu, Y. Shao, J. Wu, X. Xu, Y. Pan, H. Ju, J. Zhu and Y. Xie, *Nat. Energy*, 2019, **4**, 690–699.
38 J. Li, W. Pan, Q. Liu, Z. Chen, Z. Chen, X. Feng and H. Chen, *J. Am. Chem. Soc.*, 2021, **143**, 6551–6559.
39 C. Wen, F. Mao, Y. Liu, X. Zhang, H. Fu, L. Zheng, P. Liu and H. Yang, *ACS Catal.*, 2020, **10**, 1086–1093.
40 M. Sun, R. Gao, J. He, X. Liu, T. Nakajima, X. Zhang and L. Wang, *Angew. Chem., Int. Ed.*, 2021, **60**, 17601–17607.
41 Q. He, Y. Zhang, H. Li, Y. Yang, S. Chen, W. Yan, J. Dong, X. Zhang and X. Fan, *Small*, 2022, **18**, 2108034.
42 K. Zhang, L. Yang, Y. Hu, C. Fan, Y. Zhao, L. Bai, Y. Li, F. Shi, J. Liu and W. Xie, *Angew. Chem., Int. Ed.*, 2020, **59**, 18003–18009.

43 M. Sun, R. T. Gao, J. He, X. Liu, T. Nakajima, X. Zhang and L. Wang, *Angew. Chem., Int. Ed.*, 2021, **60**, 17601–17607.
44 Z. Wei, W. Wang, W. Li, X. Bai, J. Zhao, E. C. M. Tse, D. L. Phillips and Y. Zhu, *Angew. Chem., Int. Ed.*, 2021, **60**, 8236–8242.
45 X. Li, W. He, C. Li, B. Song and S. Liu, *Appl. Catal., B*, 2021, **287**, 119934.
46 K. Wang, Y. Du, Y. Li, X. Wu, H. Hu, G. Wang, Y. Xiao, S. Chou and G. Zhang, *Carbon Energy*, 2022, DOI: **10.1002/cey2.264**.
47 J. Liu, Y. Liu, N. Liu, Y. Han, X. Zhang, H. Huang, Y. Lifshitz, S. Lee, J. Zhong and Z. Kang, *Science*, 2015, **347**, 970–974.
48 J. Albo, M. I. Qadir, M. Samperi, J. A. Fernandes, I. de Pedro and J. Dupont, *Chem. Eng. J.*, 2021, **404**, 126643.
49 S. Cao, B. Shen, T. Tong, J. Fu and J. Yu, *Adv. Funct. Mater.*, 2018, **28**, 1800136.
50 H. Guo, J. Ding, S. Wan, Y. Wang and Q. Zhong, *Appl. Surf. Sci.*, 2020, **528**, 146943.
51 Y. X. Pan, Y. You, S. Xin, Y. Li, G. Fu, Z. Cui, Y. L. Men, F. F. Cao, S. H. Yu and J. B. Goodenough, *J. Am. Chem. Soc.*, 2017, **139**, 4123–4129.
52 G. Wang, C. T. He, R. Huang, J. Mao, D. Wang and Y. Li, *J. Am. Chem. Soc.*, 2020, **142**, 19339–19345.
53 L. Wang, Y. Wang, Y. Cheng, Z. Liu, Q. Guo, M. N. Ha and Z. Zhao, *J. Mater. Chem. A*, 2016, **4**, 5314–5322.
54 X. Wang, Y. Wang, M. Gao, J. Shen, X. Pu, Z. Zhang, H. Lin and X. Wang, *Appl. Catal., B*, 2020, **270**, 118876.
55 X. Wu, Y. Li, G. Zhang, H. Chen, J. Li, K. Wang, Y. Pan, Y. Zhao, Y. Sun and Y. Xie, *J. Am. Chem. Soc.*, 2019, **141**, 5267–5274.
56 P. Xia, M. Antonietti, B. Zhu, T. Heil, J. Yu and S. Cao, *Adv. Funct. Mater.*, 2019, **29**, 1900093.
57 W. Xiong, W. Dai, X. Hu, L. Yang, T. Wang, Y. Qin, X. Luo and J. Zou, *Mater. Lett.*, 2018, **232**, 36–39.
58 T. Yan, L. Wang, Y. Liang, M. Makaremi, T. E. Wood, Y. Dai, B. Huang, A. A. Jelle, Y. Dong and G. A. Ozin, *Nat. Commun.*, 2019, **10**, 2521.
59 Y. Zheng, Z. Duan, R. Liang, R. Lv, C. Wang, Z. Zhang, S. Wan, S. Wang, H. Xiong, C. K. Ngaw, J. Lin and Y. Wang, *ChemSusChem*, 2022, **15**, 216.
60 Y. Zheng, L. Zhang, J. Guan, S. Qian, Z. Zhang, C. K. Ngaw, S. Wan, S. Wang, J. Lin and Y. Wang, *ACS Sustainable Chem. Eng.*, 2021, **9**, 1754–1761.
61 H. Tan, Z. Zhao, W. Zhu, E. Coker, B. Li, M. Zheng, W. Yu, H. Fan and Z. Sun, *ACS Appl. Mater. Interfaces*, 2014, **6**, 19184–19190.
62 D. Ruan, S. Kim, M. Fujitsuka and T. Majima, *Appl. Catal., B*, 2018, **238**, 638–646.
63 M. A. Hossain, R. Al-Gaashani, H. Hamoudi, M. J. Al Marri, I. A. Hussein, A. Belaidi, B. A. Merzougui, F. H. Alharbi and N. Tabet, *Mater. Sci. Semicond. Process.*, 2017, **63**, 203–211.
64 L. Wang, B. Cheng, L. Zhang and J. Yu, *Small*, 2021, **17**, 2103447.
65 R. Zeng, K. Lian, B. Su, L. Lu, J. Lin, D. Tang, S. Lin and X. Wang, *Angew. Chem., Int. Ed.*, 2021, **60**, 25055–25062.
66 J. Wang, E. Kim, D. P. Kumar, A. P. Rangappa, Y. Kim, Y. Zhang and T. K. Kim, *Angew. Chem., Int. Ed.*, 2022, **61**, 202113044.
67 S. Bai, T. Li, H. Wang, L. Tan, Y. Zhao and Y.-F. Song, *Chem. Eng. J.*, 2021, **419**, 129390.
68 S. R. Docherty, N. Phongprueksathat, E. Lam, G. Noh, O. V. Safonova, A. Urakawa and C. Coperet, *J. Am. Chem. Soc.*, 2021, **1**, 450–458.
69 W. Wang, Z. Qu, L. Song and Q. Fu, *J. Energy Chem.*, 2020, **47**, 18–28.
70 H. Wang, D. Yong, S. Chen, S. Jiang, X. Zhang, W. Shao, Q. Zhang, W. Yan, B. Pan and Y. Xie, *J. Am. Chem. Soc.*, 2018, **140**, 1760–1766.